

COMPTON-THICK AGN IN THE *NuSTAR* ERA II: A DEEP *NuSTAR* AND XMM-*Newton* VIEW OF THE CANDIDATE COMPTON THICK AGN IN NGC 1358X. ZHAO¹, S. MARCHESI¹, M. AJELLO¹, L. MARCOTULLI¹, G. CUSUMANO², V. LA PAROLA², C. VIGNALI^{3,4}

Draft version March 14, 2022

ABSTRACT

We present the combined *NuSTAR* and XMM-*Newton* 0.6–79 keV spectral analysis of a Seyfert 2 galaxy, NGC 1358, which we selected as a candidate Compton thick (CT-) active galactic nucleus (AGN) on the basis of previous *Swift*/BAT and *Chandra* studies. According to our analysis, NGC 1358 is confirmed to be a CT-AGN using physical motivated models, at $>3\sigma$ confidence level. Our best-fit shows that the column density along the “line-of-sight” of the obscuring material surrounding the accreting super-massive black hole is $N_{\text{H}} = [1.96\text{--}2.80] \times 10^{24} \text{ cm}^{-2}$. The high-quality data from *NuSTAR* gives the best constraints on the spectral shape above ~ 10 keV to date on NGC 1358. Moreover, by combining *NuSTAR* and XMM-*Newton* data, we find that the obscuring torus has a low covering factor ($f_c < 0.17$), and the obscuring material is distributed in clumps, rather than uniformly. We also derive an estimate of NGC 1358’s Eddington ratio, finding it to be $\lambda_{\text{Edd}} \sim 4.7^{+0.3}_{-0.3} \times 10^{-2}$, which is in acceptable agreement with previous measurements. Finally, we find no evidence of short-term variability, over a ~ 100 ks time-span, in terms of both “line-of-sight” column density and flux.

Keywords: galaxies: active – galaxies: nuclei – galaxies: individual (NGC 1358) – X-rays: galaxies

1. INTRODUCTION

The Cosmic X-ray Background (CXB; i.e., the diffuse X-ray emission observed between 0.5 keV and 300 keV) is thought to be mainly produced by obscured and unobscured active galactic nuclei (AGN; e.g., Alexander et al. 2003; Gandhi & Fabian 2003; Gilli et al. 2007; Treister et al. 2009). Compton-thick (CT-) AGNs (with absorbing column density $N_{\text{H}} \geq \sigma_{\text{T}}^{-1} \sim 10^{24} \text{ cm}^{-2}$, where σ_{T} is the Thomson cross section) are supposed to contribute up to $\sim 10\%$ of the CXB intensity at its spectral peak (~ 30 keV, Ajello et al. 2008) and are expected to be numerous (up to 50% of the overall population of Seyfert 2 galaxies; see, e.g., Risaliti et al. 1999). However, as of today CT-AGNs have never been detected in large numbers, their observed fraction in the local Universe being $\sim 5\text{--}10\%$ (see, e.g., Burlon et al. 2011; Ricci et al. 2015), significantly below the predictions of different CXB models ($\sim 20\%\text{--}30\%$, see Ueda et al. 2014, and references therein). Nevertheless, it has been suggested that the small observed fraction of heavily obscured AGN observed can be caused by the bias in detecting CT-AGN in X-rays, even sampling the energy range above 10 keV (see, e.g. Burlon et al. 2011). Efforts to correct for this observational bias have recovered a fraction of $\sim 20\%$ of CT-AGN, under some assumptions (see, e.g., Burlon et al. 2011; Brightman & Nandra 2011; Ricci et al. 2015).

In Compton-thick AGN, the spectrum is significantly suppressed at energies ≤ 10 keV (Gilli et al. 2007; Koss

et al. 2016) and the overall emission is dominated by the Compton hump at $\sim 30\text{--}50$ keV. Consequently, CT-AGNs at redshifts $z > 1$ can be studied using one of the several facilities sampling the $\sim 0.5\text{--}10$ keV energy range, such as XMM-*Newton*, *Chandra*, *Swift*-XRT and *Suzaku* (see, e.g., Georgantopoulos et al. 2013; Buchner et al. 2015; Lanzuisi et al. 2015), since the Compton hump of high- z sources is redshifted in the energy range covered by these instruments. For sources in the local Universe ($z < 0.1$), however, the proper characterization of heavily obscured AGN requires an X-ray telescope sensitive above 10 keV. Thanks to the launch of *Nuclear Spectroscopic Telescope Array* (hereafter, *NuSTAR*, Harrison et al. 2013), which provides a two orders of magnitude better sensitivity than previous telescopes at these energies (e.g., *INTEGRAL* and *Swift*/BAT; Winkler et al. 2003; Barthelmy et al. 2005), we can characterize the physical properties of heavily obscured AGN with unprecedented accuracy (see, e.g., Baloković et al. 2014; Puccetti et al. 2014; Annular et al. 2015; Marchesi et al. 2017b; Ursini et al. 2018). However, since a typical highly obscured AGN spectrum barely depends on the column density at > 10 keV but varies considerably at < 10 keV (see, e.g., Gilli et al. 2007), it is difficult to constrain the column density with *NuSTAR* alone. Consequently, XMM-*Newton*, as the best instrument in terms of effective area in 0.3–10 keV (~ 10 times larger than *Swift*-XRT and ~ 2 times larger than *Chandra*), is the ideal instrument to complement *NuSTAR* strength in characterizing heavily obscured AGNs.

Indeed, the study of single targets using *NuSTAR* or combining *NuSTAR* and other lower-energy X-ray observatories (e.g., XMM-*Newton* and *Chandra*) has already been shown to be strategic to characterize heavily obscured AGN, and understand their physical properties. For example, NGC 1448 was observed and identified as a CT-AGN in X-rays for the first time using *NuSTAR*

¹ Department of Physics & Astronomy, Clemson University, Clemson, SC 29634, USA

² INAF - Istituto di Astrofisica Spaziale e Fisica Cosmica, Via U. La Malfa 153, I-90146 Palermo, Italy

³ INAF-Osservatorio Astronomico di Bologna, Via Piero Gobetti, 93/3, 40129, Bologna, Italy

⁴ Dipartimento di Fisica e Astronomia, Alma Mater Studiorum, Università di Bologna, Via Piero Gobetti, 93/2, 40129, Bologna, Italy

and *Chandra* (Annuar et al. 2017). The source was too faint (intrinsic 2–10 keV luminosity $L_{\text{int},2-10 \text{ keV}} = 3.5\text{--}7.6 \times 10^{40} \text{ erg s}^{-1}$) to be identified by *Swift*/BAT, even using its deepest 104 month maps, and was only detected in one out of five *Swift*-XRT observations. Another example is the analysis of NGC 1068 reported in Bauer et al. (2015). In this work, the authors used *NuSTAR* to characterize with unprecedented quality this largely studied CT-AGN, putting much stronger constraints on the high-energy spectral shape of NGC 1068.

The obscuration observed in AGN across the electromagnetic spectrum, from the X-ray, to the optical and infrared, is usually explained with a pc-scale, torus-like structure of dust and gas (see, e.g., Almeida & Ricci 2017). Consequently, in the past two decades several tori models, based on Monte Carlo simulations, have been developed to characterize CT-AGN X-ray spectra (Matt & Fabian 1994; Ikeda et al. 2009; Murphy & Yaqoob 2009; Brightman & Nandra 2011; Liu & Li 2014; Furui et al. 2016; Baloković et al. 2018). All these models assume a continuous distribution of the obscuring material, but with different assumption on the geometry of the torus. In particular, in the models proposed by Ikeda et al. (2009), Brightman & Nandra (2011) and Baloković et al. (2018), the half opening angle of torus, i.e., the torus covering factor, is a free parameter, thus allowing to put constraints on the typical tori geometry. Given the intrinsic complexity of these models, and the multiple free parameters involved, using them in full capacity requires high-quality X-ray spectra, with excellent statistics on a wide energy range, i.e., between 2 and 100 keV: as of today, such requirements can be satisfied only by a joint *NuSTAR* and *XMM-Newton* observation.

In this work we present the results of a deep, 50 ks joint *NuSTAR* and *XMM-Newton* observation of NGC 1358, a nearby Seyfert 2 galaxy and a CT-AGN candidate. The paper is organized as follows: in Section 2 we present the selection technique that brought us to classify NGC 1358 as a new candidate CT-AGN, and we report the *NuSTAR* and *XMM-Newton* data reduction and spectral extraction process. In Section 3, we describe the different models, both phenomenologicals and physicals, which have been used to fit the spectra, and the results of the spectral analysis. In Section 4 we compare our results with previous ones, derive the source Eddington ratio and discuss the constraints on the geometry and clumpiness of the obscuring materials. All reported errors are at 90% confidence level, if not otherwise stated. Standard cosmological constants are adopted as follows: $\langle H_0 \rangle = 70 \text{ km s}^{-1} \text{ Mpc}^{-1}$, $\langle q_0 \rangle = 0.0$ and $\langle \Lambda \rangle = 0.73$.

2. OBSERVATION AND DATA ANALYSIS

NGC 1358 ($z \sim 0.013436$, Theureau et al. 1998), is a Seyfert 2 galaxy detected in the 100-month BAT catalog (with a 7.8σ significance; Segreto et al. 2018 in prep.), a catalog of ~ 1000 AGN detected by *Swift*-BAT in the 15–150 keV band.

In Marchesi et al. (2017a), we describe a technique developed to select highly obscured AGN candidates from the BAT sample, using the following criteria:

1. Lack of a 0.5–2.4 keV, *ROSAT*/RASS (Boller et al. 2016) counterpart. For objects located outside the

Galactic plane (i.e., having Galactic latitude $|b| > 10$ deg), the lack of *ROSAT* counterparts already implies a minimum AGN column density $\log(N_{\text{H}}) \sim 23$ (see, e.g., Figure 2 in Koss et al. 2016).

2. Seyfert 2 galaxy optical classification, i.e., the source must have an optical spectrum without broad ($\text{FWHM} \geq 2000 \text{ km s}^{-1}$) emission lines. It has been shown (see, e.g., Marchesi et al. 2016, and references therein) that Seyfert 2 galaxies are more likely to be obscured than Seyfert 1 ones. Furthermore, there are no known Seyfert 1 galaxy that are Compton thick⁵ (see, e.g., Ricci et al. 2015).
3. Low redshift ($z < 0.04$). Due to selection effects, the vast majority of BAT-selected CT-AGNs are detected in the nearby Universe: for example, 47 out of 55 CT-AGNs reported in Ricci et al. (2015) are located at $z < 0.04$.

Following these criteria, we obtained a snapshot (10 ks) *Chandra* observation for a sample of seven sources, and we performed a first measurement of their fundamental spectral parameters, particularly the power law photon index, Γ , and the column density, N_{H} . NGC 1358 was found to be the most obscured object in our sample, having “line-of-sight” column density $N_{\text{H}} = 1.05_{-0.36}^{+0.42} \times 10^{24} \text{ cm}^{-2}$, thus making it a candidate CT-AGN, although only at a 1σ confidence level, due to the low-quality of the *Chandra* spectrum.

To further investigate this new candidate CT-AGN we proposed for a joint deep *NuSTAR* (50 ks) and *XMM-Newton* (48 ks) follow-up observation, which was accepted in *NuSTAR* Cycle 3 (proposal ID 3258, PI: Marchesi). We report a summary of the two observations in Table 1.

2.1. *NuSTAR* Observation

NGC 1358 was observed by *NuSTAR* on 2017 August 1 (ObsID 60301026002): the net exposure time is 50 ks. The observation actually took place in a 96.9 ks time-span and was divided in 16 (~ 3 ks) intervals. The non-exposed time between each interval is when the target is occulted by the Earth.

The *NuSTAR* data are derived from both focal plane modules, FPMA and FPMB. The raw files are calibrated, cleaned and screened using the *NuSTAR* *nupipeline* script version 0.4.5. The *NuSTAR* calibration database (CALDB) used in this work is the version 20161021. The ARF, RMF and light-curve files are obtained using the *nuproducts* script.

For both modules, the source spectrum is extracted from a $25''$ circular region, corresponding to $\approx 40\%$ of the encircled energy fraction at 10 keV, centered on the source optical position. We then extract a background spectrum for each module, choosing a $30''$ circular region located nearby the outer edges of the field of view, to avoid contamination from NGC 1358. We group the *NuSTAR* spectra with a minimum of 15 counts per bin with *grppha* task. The signal of both modules is $> 3\sigma$ in 3–79 keV band.

⁵ there are sources which are Compton-thick but with ambiguous activity classification, e.g. NGC 424 (a.k.a. Tololo0109-383)

Table 1
Summary of *NuSTAR* and XMM-*Newton* observation.

Instrument	Sequence ObsID	Start Time (UTC)	End Time (UTC)	Exposure Time (ks)	Count Rate ^a $10^{-2} \text{ counts s}^{-1}$
<i>NuSTAR</i>	60301026002	2017-08-01T03:41:09	2017-08-02T06:36:09	50	2.32 ± 0.07 2.28 ± 0.07
XMM- <i>Newton</i>	0795680101	2017-08-01T17:05:27	2017-08-02T06:03:10	48	0.98 ± 0.05 0.91 ± 0.05 3.68 ± 0.15

^aThe reported *NuSTAR* net count rates are those of the FPMA and FPMB modules between 3–79 keV, respectively. The reported XMM-*Newton* net count rates are those the MOS1, MOS2 and pn modules in 0.6–10 keV, respectively.

2.2. XMM-Newton Observation

The XMM-*Newton* observation was taken quasi-simultaneously to the *NuSTAR* one starting ~ 12 hours after the *NuSTAR* one, but ending at the same time (due to the gaps between observing intervals in *NuSTAR*). XMM-*Newton* data have been reduced using the Science Analysis System (SAS; Jansen et al. 2001) version 16.1.0. 13 ks of XMM-*Newton* modules MOS1 and MOS2 and 30 ks of pn observations were affected by a strong background flare, therefore we decided to exclude that part of observation from our analysis. Consequently, the total net XMM-*Newton* exposure time of our observation is 101 ks. The source spectra are extracted from a $15''$, corresponding to $\approx 70\%$ of the encircled energy fraction at 1.5 keV, circular region, while the background spectra are from a $80''$ circle located nearby the source. We visually inspected the XMM-*Newton* image to avoid contamination to the background from sources nearby NGC 1358. All three modules, MOS1, MOS2 and pn are jointly used in the spectral modeling, and their normalization are tied together assuming their cross-calibration uncertainties are marginal.

3. SPECTRAL MODELING RESULTS

We use XSPEC (Arnaud 1996) v12.9.1 to fit the spectrum and rely on the χ^2 statistic for the optimization of the spectral fit. The photoelectric cross section for all absorption components used here are derived from Verner et al. (1996), adopting an element abundance from Anders & Grevesse (1989). The Galactic absorption column density is $N_{\text{H}}^{\text{Gal}} = 3.83 \times 10^{20} \text{ cm}^{-2}$ (Kalberla et al. 2005). The metal abundance is fixed to Solar.

Following a standard approach in analyzing heavily obscured AGN, we first fit our data using different phenomenological models, particularly the **pexrav** one (Magdziarz & Zdziarski 1995). We then move to more accurate self-consistent models, based on Monte Carlo simulations, which are specifically developed to treat the spectra of heavily obscured AGN: the physical models we use in this work are **MYTorus** (Murphy & Yaqoob 2009) and **borus02** (Baloković et al. 2018). We report the results of our analysis in the following sections.

3.1. Phenomenological Models

3.1.1. Absorbed power law

We initially fit our data with a simple phenomenological model, comprising a power law (*zpowerlw* in XSPEC) absorbed by intervening gas modeled with (*zphabs*). We also add a Gaussian (*zgauss*) to model the Fe $K\alpha$ fluorescent emission line ($E_{K\alpha} = 6.4 \text{ keV}$); we assume the line to be narrow, fixing the line width σ to 50 eV, since there is no statistical improvement in fits if the parameter is left free to vary. We also add a second, unabsorbed power

law, to model the fractional AGN emission, which is not intercepted by the torus on the “line-of-sight”, and/or the scattering emission that is deflected, rather than absorbed by the obscuring material. Here, and elsewhere in the paper, the photon index of the scattered component is tied to the one of the main power law. The scattered component is usually less than 5–10% of the main one (see, e.g., Marchesi et al. 2018). We denote this fraction as f_s , and we model it with a constant (*constant2*). Furthermore, we add to the fit a thermal component, namely *mekal* (Mewe et al. 1985), to model the soft excess observed below 1 keV, and potentially due to either star-formation processes and/or thermal emission from a hot interstellar medium. The temperature and the relative metal abundance in *mekal* are both left free to vary.

The first model (hereafter, “Model A”), in XSPEC nomenclature, is therefore:

$$\text{Model A} = \text{constant}_1 * \text{phabs} * (\text{zphabs} * \text{zpowerlw} + \text{zgauss} + \text{constant}_2 * \text{zpowerlw} + \text{mekal}) \quad (1)$$

where *constant*₁ represents the cross calibration between different instruments, noted as $C_{\text{NuS}/\text{XMM}}$. In our fits, the cross-calibration between different modules of the same instrument is fixed to 1. *phabs* is applied here to model the Galactic absorption.

We report in Table 2 the best-fit results for the simple phenomenological model applied to the joint *NuSTAR*–XMM-*Newton* spectrum. The best-fit photon index is $\Gamma = 1.14_{-0.12}^{+0.13}$; the column density is $N_{\text{H}} = 0.95_{-0.11}^{+0.11} \times 10^{24} \text{ cm}^{-2}$. While the best-fit reduced χ^2 of model A is statistically acceptable, being $\chi^2_{\nu} = \chi^2/\text{degree of freedom}$ (d.o.f. hereafter) = 256/240 = 1.07, standard absorption components in XSPEC, such as *zphabs*, fail to characterize the spectral complexity of heavily obscured AGN like NGC 1358 properly. Therefore, a more physical model needs to be applied.

3.1.2. Including a reflection component

Obscured AGNs X-ray spectra have historically been modeled using the **pexrav** model (Magdziarz & Zdziarski 1995). **pexrav** is used to model an exponentially cut-off power law spectrum reflected from neutral slab. We first test the model with a pure reflector by setting the reflection scaling factor in **pexrav** to be $R = -1$: this models a heavily obscured ($N_{\text{H}} > 10^{25} \text{ cm}^{-2}$) source whose spectrum is dominated by the reflection from the “back-side” of the torus. The fit shows that photon index is $\Gamma = 1.30_{-0.05}^{+0.05}$ and $\chi^2/\text{d.o.f} = 349/242$. Such a large reduced χ^2 suggests that a pure reflector is not enough to describe the spectrum. Therefore, we follow the method described in, e.g., Ricci et al. (2011) by using the complete **pexrav** model, which includes an intrinsic cut-off

power law by setting the reflection scaling factor R to be greater than 0.

The model in **XSPEC** is described as follows:

$$\text{ModelB} = \text{constant}_1 * \text{phabs} * (\text{zphabs} * \text{pexrav} + \text{zgauss} + \text{constant}_2 * \text{zpowerlw} + \text{mekal}) \quad (2)$$

The components are those described previously in Section 3.1.1, except for the main power law, which is replaced by **pexrav**. The inclination angle i , i.e., the angle between the axis of the AGN (normal to the disk) and the observer “line-of-sight”, which is a free parameter in **pexrav**, is fixed at $i = 60^\circ$ (i.e. $\cos i = 0.5$): we find no significant change in the best-fit statistic and in the other parameters when allowing i to vary. The cut-off energy of **pexrav** is fixed at 500 keV, to be consistent with the **MYTorus** model, which we will extensively discuss in the following section.

When leaving the reflection scaling factor R in **pexrav** free to vary, we obtain a best-fit value of $R > 4$ (such a large reflection scaling factor is also found by Ricci et al. 2011, in heavily obscured AGN), although we are not able to put any constraint on the parameter 90% confidence uncertainties. Such a result would point towards a “reflection-dominated” scenario, where most of the observed emission comes from the reflected component, while the direct emission from the accreting SMBH is absorbed by the heavily obscuring material along the “line of sight”. A larger scaling factor can also be interpreted as the geometry of reflected material is more like a torus rather than a disk⁶. Since R is not constrained when left free to vary, we decided to complete our spectral analysis fixing the reflection scaling parameter to $R = 4$. Here we are modeling a process that the intrinsic emission together with the reflection from the “back-side” are obscured by the same circumnuclear material.

We report in Table 2 the best-fit parameters for the analysis of the joint *NuSTAR*–*XMM-Newton* spectra using model B. The photon index is $\Gamma = 1.59^{+0.11}_{-0.11}$. The best-fit column density is $N_H = 0.76^{+0.09}_{-0.09} \times 10^{24} \text{ cm}^{-2}$. In agreement with what we found using Model A, the source is near the threshold of CT-AGN. We present the unfolded *NuSTAR* and *XMM-Newton* spectrum of NGC 1358, fitted with the model B and ratio between data and model, in figure 1.

In summary, both phenomenological models suggest that obscuration is near the Compton-thick threshold, such that the source cannot be confirmed as CT-AGN at $>3\sigma$ confidence level. However, the photon indices obtained above are far from the typical value observed in AGN ($\Gamma \sim 1.8$, see, e.g., Marchesi et al. 2016), showing that some components may not be well described by the above phenomenological models. Therefore, more physically motivated models are needed to describe the spectra and extract the physical and geometrical properties of NGC 1358.

3.2. Physical Models

3.2.1. MYTorus

⁶ as a larger value of the scaling factor represents a larger amount of reflected material, thus the reflected material is more torus-like rather than disk-like geometrically.

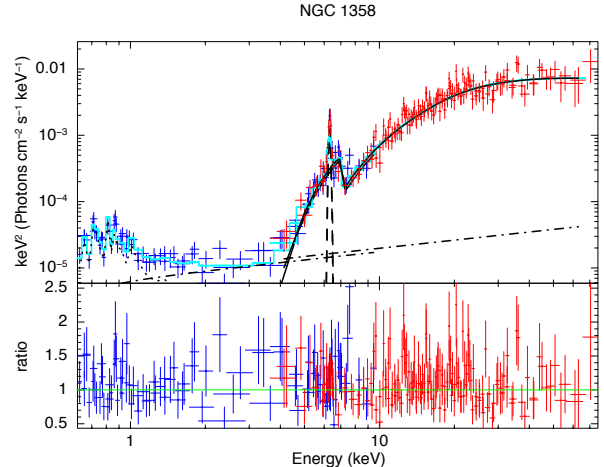


Figure 1. Unfolded *XMM-Newton* and *NuSTAR* spectrum of NGC 1358 fitted with the **pexrav** model (top) and ratio between data and model (bottom). The *XMM-Newton* data is plotted in blue, while the *NuSTAR* data is plotted in red. The best-fit models prediction is plotted as a cyan solid line. The single components of the model are plotted in black with different line styles, i.e., the absorbed intrinsic continuum as a solid line, the reflection component and Fe $K\alpha$ line as a dashed line, the scattered component as a dash-dotted line and the *mekal* component as a dotted line.

The first physically motivated model applied in our analysis is **MYTorus** (Murphy & Yaqoob 2009; Yaqoob 2012; Yaqoob et al. 2015). The basic geometry of **MYTorus** model consists of a torus that has a fixed half-opening angle, $\theta = 60^\circ$, with a circular cross section.

An advantage of the physically motivated **MYTorus** model is that the main components observed in the spectrum of an obscured AGN can be treated self-consistently. More in detail, **MYTorus** model is composed of three parts: the direct continuum, the Compton-scattered component and fluorescent lines. The direct continuum, which is also called zeroth-order continuum, is the “line-of-sight” observed continuum, i.e., the intrinsic X-ray continuum as observed after the absorption caused by the torus. In **MYTorus**, this first component is a multiplicative factor (a multiplicative table in **XSPEC**), which is applied to the intrinsic continuum. The second component is the scattered continuum and it models those photons that are Compton-scattered into the observer “line-of-sight” by the gas in the environment of the SMBH. If the covering factor of the torus differs significantly from the fixed **MYTorus** value, $f_c = \cos(\theta) = 0.5$, or if there is a non-negligible time delay between the intrinsic continuum emission and the Compton-scattered continuum one, i.e., the center region is not compact and the intrinsic emission varies rapidly, the two components could have different normalizations. To take these effects into account, the scattered continuum is multiplied by a relative normalization, which is noted as A_S (Yaqoob 2012). Finally, the third component models the most prominent fluorescent lines, i.e., the Fe $K\alpha$ and Fe $K\beta$ lines, at 6.4 keV and 7.06 keV, respectively. Analogously to A_S , the relative normalization between the fluorescent lines and direct continuum is noted as A_L . In **XSPEC**, A_S and A_L are implemented as two *constant* components before the additive tables, while the normalization of the three components are set to be the same. Following pre-

Table 2
Summary of Best-Fits of XMM-Newton and NuSTAR Data using Different Models

Model	phenom	pexrav	MYTorus (coupled)	MYTorus (decoupled face on)	MYTorus (decoupled edge on)	borus02
χ^2/dof	256/240	231/240	231/239	230/239	220/239	222/238
C_{Ins}^a	$1.06^{+0.14}_{-0.12}$	$1.13^{+0.14}_{-0.13}$	$1.12^{+0.15}_{-0.20}$	$1.13^{+0.15}_{-0.13}$	$1.17^{+0.16}_{-0.14}$	$1.16^{+0.12}_{-0.14}$
Γ	$1.14^{+0.13}_{-0.12}$	$1.59^{+0.11}_{-0.11}$	$1.52^{+0.17}_{-*}$	$1.66^{+0.15}_{-0.26}$	$1.85^{+0.13}_{-0.23}$	$1.79^{+0.13}_{-0.04}$
N_H^b	$0.95^{+0.11}_{-0.11}$	$0.76^{+0.09}_{-0.09}$
$\text{norm}^c 10^{-2}$	$0.03^{+0.02}_{-0.01}$	$0.04^{+0.02}_{-0.01}$	$0.13^{+0.16}_{-0.06}$	$0.20^{+0.24}_{-0.13}$	$1.61^{+1.26}_{-1.08}$	$1.26^{+0.79}_{-0.04}$
$N_{H,\text{eq}}$	$3.02^{+2.54}_{-1.12}$
θ_{Tor}^d	$84.0^{+*}_{-3.9}$
θ_{Obs}	$62.53^{+4.33}_{-2.53}$	$87.1^{+*}_{-0.3}$
A_S	$1.03^{+0.55}_{-0.51}$	$0.78^{+0.47}_{-0.26}$	$0.23^{+0.18}_{-0.06}$...
$N_{H,Z}$	$1.19^{+0.27}_{-0.22}$	$2.40^{+0.40}_{-0.44}$	$2.40^{+0.39}_{-0.12}$
$N_{H,S}$	$5.25^{+*}_{-2.26}$	$0.50^{+0.12}_{-0.09}$	$0.65^{+0.05}_{-0.16}$
$f_s 10^{-2}$	$1.69^{+0.70}_{-0.51}$	$1.92^{+0.76}_{-0.57}$	$0.08^{+0.14}_{-0.08}$	$0.12^{+0.36}_{-0.12}$	$0.05^{+0.02}_{-0.07}$	$0.05^{+0.01}_{-0.01}$
kT^e	$0.49^{+0.09}_{-0.13}$	$0.49^{+0.10}_{-0.15}$	$0.58^{+0.07}_{-0.10}$	$0.57^{+0.07}_{-0.12}$	$0.58^{+0.06}_{-0.12}$	$0.52^{+0.06}_{-0.11}$
abund^f	$0.05^{+0.08}_{-0.04}$	$0.07^{+0.19}_{-0.05}$	$0.03^{+0.04}_{-0.02}$	$0.04^{+0.05}_{-0.02}$	$0.11^{+18.29}_{-0.08}$	$0.05^{+0.08}_{-0.03}$
F_{2-10}^g	$4.18^{+0.23}_{-0.59}$	$4.09^{+0.26}_{-0.68}$	$4.03^{+100.}_{-2.99}$	$4.03^{+0.19}_{-3.21}$	$3.84^{+0.28}_{-1.75}$	$3.87^{+1.11}_{-3.86}$
F_{10-40}^h	$8.22^{+0.27}_{-1.56}$	$8.68^{+0.28}_{-0.94}$	$8.48^{+7.99}_{-8.48}$	$8.55^{+0.13}_{-3.77}$	$8.51^{+0.26}_{-2.48}$	$8.51^{+0.46}_{-8.51}$
L_{2-10}^i	$0.116^{+0.005}_{-0.004}$	$0.07^{+0.01}_{-0.01}$	$0.28^{+0.02}_{-0.02}$	$0.34^{+0.03}_{-0.02}$	$2.06^{+0.11}_{-0.11}$	$1.77^{+0.10}_{-0.11}$
L_{10-40}^j	$0.36^{+0.01}_{-0.02}$	$0.11^{+0.12}_{-0.11}$	$0.48^{+0.04}_{-0.03}$	$0.49^{+0.03}_{-0.03}$	$2.23^{+0.12}_{-0.12}$	$2.09^{+0.12}_{-0.12}$

Note. — We summarize here the best-fits of joint *NuSTAR*–*XMM-Newton* spectra using different models referred in section 3. We also report the statistics and degree of freedom for each fit.

^a $C_{Ins} = C_{NuS/XMM}$ is the cross calibration between *NuSTAR* and *XMM-Newton*.

^b“line-of-sight” column density in phenomenological models in 10^{24} cm^{-2}

^cnormalization of components in different models at 1 keV in photons $\text{keV}^{-1} \text{ cm}^{-2} \text{ s}^{-1}$.

^dangle between the axis of the torus and the edge of torus in degree, where the covering factor $f_c = \cos(\theta_{\text{Tor}})$.

^etemperature in the thermal component *mekal* in keV.

^fabundance in the thermal component *mekal*.

^gFlux between 2–10 keV in $10^{-13} \text{ erg cm}^{-2} \text{ s}^{-1}$.

^hFlux between 10–40 keV in $10^{-12} \text{ erg cm}^{-2} \text{ s}^{-1}$.

ⁱIntrinsic luminosity between 2–10 keV in $10^{43} \text{ erg s}^{-1}$.

^jIntrinsic luminosity between 10–40 keV in $10^{43} \text{ erg s}^{-1}$.

vious works, the two relative normalizations are set to be equal, i.e., $A_S = A_L$.

In *XSPEC* our model is described as follows:

$$\begin{aligned}
 \text{ModelC} = & \text{constant}_1 * \text{phabs} * \\
 & (\text{mytorus_Ezero.v00.fits} * \text{zpowerlw} \\
 & + A_S * \text{mytorus_scatteredH500.v00.fits} \\
 & + A_L * \text{mytl_V000010nEp000H500.v00.fits} \\
 & + \text{constant}_2 * \text{zpowerlw} + \text{mekal})
 \end{aligned} \tag{3}$$

where table *mytorus_Ezero.v00.fits* is the zeroth-order continuum component, *mytorus_scatteredH500.v00.fits* accounts for the scattered continuum, and *mytl_V000010nEp000H500.v00.fits* models the fluorescent lines.

The **MYTorus** model can be used in two different configurations, named ‘coupled’ and ‘decoupled’ (Yaqoob 2012). We test both of them on our data, and we report the results in the following sections.

3.2.2. MYTorus in ‘coupled’ configuration

In **MYTorus**, the angle between the axis of the torus and the “line-of-sight”, the so-called “torus inclination

angle”, is a free parameter, that we hereafter define as θ_{obs} . The inclination angle varies in the range $\theta_{\text{obs}} = [0-90]^\circ$, where $\theta_{\text{obs}} = 0^\circ$ models a torus observed “face-on”, and $\theta_{\text{obs}} = 90^\circ$ is observed “edge-on”. In the ‘coupled’ configuration, θ_{obs} is set to be the same for all three **MYTorus** components.

We report in Table 2 the best-fit parameters obtained using the **MYTorus** ‘coupled’ model. We fit the *XMM-Newton* data in the 0.6–10 keV energy range to avoid a known **MYTorus** fit issue below 0.6 keV, that may cause large statistical errors (more details are available in the **MYTorus** manual⁷). The best-fit photon index is $\Gamma = 1.52^{+0.17}_{-*}$ (the lower limit of the photon index cannot be constrained in our modeling since it falls below 1.4, the value that is the smallest value that can be tested with **MYTorus**). The photon index of the Compton-scattered continuum and of the iron emission feature component set to be the same with that of direct continuum. The equatorial column density is $N_{H,\text{eq}} = 3.02^{+2.54}_{-1.12} \times 10^{24} \text{ cm}^{-2}$. The inclination angle is $\theta_{\text{obs}} = 62.53^{+4.33}_{-2.53}^\circ$, suggesting that we are observing through

⁷ <http://mytorus.com/mytorus-instructions.html>

the ‘brink’ of the torus. The “line-of-sight” column density is defined as $N_{\text{H,l.o.s.}} = N_{\text{H,eq}} [1 - 4 \cos^2 \theta_{\text{obs}}]^{1/2} = 1.17^{+3.94}_{-1.17} \times 10^{24} \text{ cm}^{-2}$. The reduced χ^2 is $\chi^2_\nu = 231/239 = 0.97$.

3.2.3. MYTorus in ‘decoupled’ configuration

The ‘decoupled’ MYTorus model, which is first introduced in Yaqoob (2012), adds flexibility to the MYTorus model as it allows the users to model the absorber’s structure with a more general geometry and even simulate a clumpy distribution of the obscuring material. In this configuration, the direct continuum is a pure “line-of-sight” quantity, and the inclination angle of the direct continuum is fixed to $\theta_{\text{obs,Z}} = 90^\circ$, such that the column density of the direct continuum models the “line-of-sight” column density, $N_{\text{H,Z}}$. The inclination angle of the Compton-scattered continuum and fluorescent lines is instead set to be either observed “face-on”, such that $\theta_{\text{obs,S,L}} = 0^\circ$, or observed “edge-on”, i.e., $\theta_{\text{obs,S,L}} = 90^\circ$. The “face-on” configuration mimics the reprocessed emission coming from the “back-side” of the torus, which is expected to be more prominent in a patchy, less uniform torus, where the photons emitted by the “back-side” of the torus have a smaller chance of being absorbed before reaching the observer. In the “edge-on” scenario, instead, the photons are reprocessed by the obscuring material lying between the AGN and the observer, and an “edge-on-dominated” reprocessed emission therefore favors a more uniform distribution of the obscuring material. In the ‘decoupled’ MYTorus model, the column density of the scattered continuum and of the fluorescent lines, $N_{\text{H,S}}$, describes the “global average” column density of the torus, i.e., the average column density of the obscuring material, which can significantly differ from the “line-of-sight” value in an inhomogeneous, patchy torus.

In Yaqoob (2012), the ‘decoupled’ MYTorus model is used adding to the model both the $\theta_{\text{obs,S,L}} = 90^\circ$ and the $\theta_{\text{obs,S,L}} = 0^\circ$ reprocessed components, thus we first test this model, where both components contribute to the total reprocessed emission. In such a scenario, the best-fit is $\chi^2/\text{d.o.f} = 222/238 = 0.93$, while the intensity of the “face-on” component is 15 times smaller than the intensity of the “edge-on” component, suggesting that the reprocessed emission in NGC 1358 comes mostly from material located between the AGN and the observer. For this reason, following the approach described in Yaqoob et al. (2015), we re-fit our data twice, each time using only one of the two reprocessed component configurations. The best-fit for the pure “back-side” reflection model, i.e., $\theta_{\text{obs,S,L}} = 0^\circ$ is presented in Table 2. The photon index is $\Gamma_{\theta,\text{S}=0} = 1.66^{+0.15}_{-0.26}$, the “line-of-sight” column densities is $N_{\text{H,Z},\theta,\text{S}=0} = 1.19^{+0.27}_{-0.22} \times 10^{24} \text{ cm}^{-2}$ and the “global average” column density is $N_{\text{H,S},\theta,\text{S}=0} = 5.25^{+*}_{-2.26} \times 10^{24} \text{ cm}^{-2}$. The best-fit by using only the $\theta_{\text{obs,S,L}}=90^\circ$ is also presented in Table 2. The photon index is $\Gamma_{\theta,\text{S}=90} = 1.85^{+0.13}_{-0.23}$. The “line-of-sight” column densities is $N_{\text{H,Z},\theta,\text{S}=90} = 2.40^{+0.40}_{-0.44} \times 10^{24} \text{ cm}^{-2}$. The “global average” column density is $N_{\text{H,S},\theta,\text{S}=90} = 0.50^{+0.12}_{-0.09} \times 10^{24} \text{ cm}^{-2}$. The “global average” column density is a few times smaller than the “line-of-sight” column density, suggesting a patchy torus scenario, where

the AGN is observed through an over-dense cloud.

In conclusion, the best-fit of ‘decoupled’ MYTorus model in both “face-on” and “edge-on” configurations confirm the Compton-thick origin of NGC 1358 at 3σ confidence level. The MYTorus ‘decoupled’ model in “edge on” configuration produced the best-fit, $\chi^2_\nu = \chi^2/\text{d.o.f} = 220/239 = 0.92$ and most reasonable photon index ($\Gamma \sim 1.8$, see, e.g., Marchesi et al. 2016), among all the models and is thus our favorite model. Figure 2 shows the unfolded *NuSTAR* and *XMM-Newton* spectrum of NGC 1358, fitted with the ‘decoupled’ MYTorus model in “edge on” configuration.

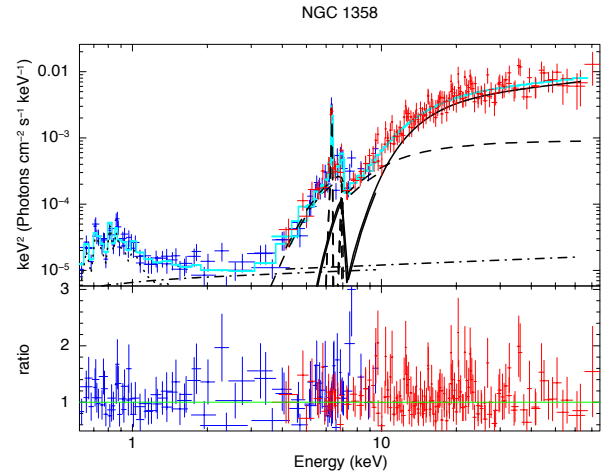


Figure 2. Unfolded XMM-Newton and *NuSTAR* spectrum of NGC 1358, fitted with the ‘decoupled’ MYTorus model in “edge on” configuration (top) and ratio between data and model (bottom). The XMM-Newton data is plotted in blue, while the *NuSTAR* data is plotted in red. The best-fit model prediction is plotted as a cyan solid line. The single components of the model are plotted in black with different line styles, i.e., the absorbed intrinsic continuum as a solid line, the Compton-scattered continuum and the fluorescent lines as a dashed line, the scattered component as a dash-dotted line and the *mekal* component as a dotted line.

3.2.4. BORUS02

While MYTorus is known to be effective in modeling the X-ray spectra of heavily obscured AGN, it assumes a fixed torus opening angle ($\theta_{\text{Tor}} = 60^\circ$, i.e., a covering factor $f_c = \cos \theta_{\text{Tor}} = 0.5$), limiting the model to a single torus geometry in ‘coupled’ mode and do not allowing one to directly measure the covering factor even in the ‘decoupled’ mode, although the latter can be in principle used to mimic different geometries of the obscuring material. To complement our analysis, we therefore fit the NGC 1358 spectrum using the recently published *borus02* model (Baloković et al. 2018), an updated version of the so-called *BNTorus* model (Brightman & Nandra 2011). In *borus02* the torus covering factor is a free parameter varying in range of $f_c = [0.1-1]$, corresponding to a torus opening angle $\theta_{\text{Tor}} = [0-84]^\circ$.

`borus02` is used in the following `XSPEC` configuration:

$$\text{ModelD} = \text{constant}_1 * \text{phabs} * (\text{borus02.v170323a.fits} \\ + \text{zphabs} * \text{cabs} * \text{zpowerlw} + \text{constant}_2 * \\ \text{zpowerlw} + \text{mekal}) \quad (4)$$

where `borus02.v170323a.fits` is an additive table that models the reprocessed components, including the fluorescent line emission and the reprocessed continuum. The “line-of-sight” absorption is modeled by the `zphabs` \times `cabs` including Compton scattering lost out of the “line-of-sight”, that includes the effect of Compton scattering. The other components are similar to `MYTorus`.

The best-fit results are presented in Table 2. The photon index is $\Gamma = 1.79^{+0.13}_{-0.04}$. The “line-of-sight” column density is $N_{\text{H,Z}} = 2.40^{+0.39}_{-0.12} \times 10^{24} \text{ cm}^{-2}$, while the column density of the torus is $N_{\text{H,S}} = 0.65^{+0.05}_{-0.16} \times 10^{24} \text{ cm}^{-2}$, which is in good agreement with the results of the `MYTorus` ‘decoupled’ model in “edge on” configuration. The covering factor of the torus is $f_c < 0.17$, i.e., a disk-like torus, which is strongly different from the setup of `MYTorus` model, which will be further discussed in section 4. Finally, the angle between the torus axis and the observer “line-of-sight” is $\theta_{\text{obs}} > 86.8^\circ$, suggesting that the ‘edge on’ scenario is favored. Figure 3 shows the unfolded XMM-*Newton* and *NuSTAR* spectrum of NGC 1358, fitted by the `borus02` model.

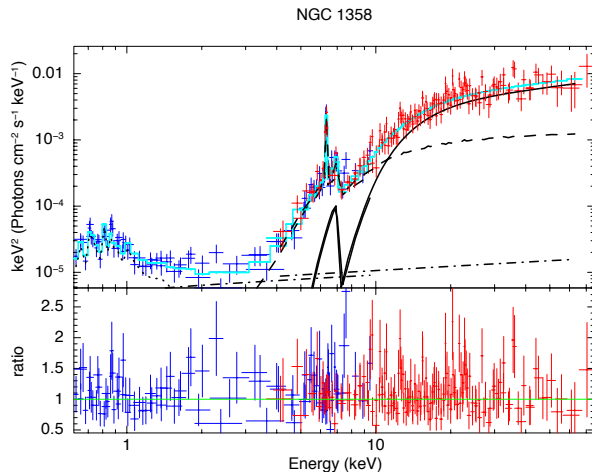


Figure 3. Unfolded XMM-*Newton* and *NuSTAR* spectrum of NGC 1358, fitted with the `borus02` model (top) and ratio between data and model (bottom). The XMM-*Newton* data is plotted in blue, while the *NuSTAR* data is plotted in red. The best-fit model prediction is plotted as a cyan solid line. The single components of the model are plotted in black with different line styles, i.e., the absorbed intrinsic continuum as a solid line, the reflection component and fluorescent lines as a dashed line, the scattered component as a dash-dotted line and the `mekal` component as a dotted line.

3.3. Summary of the spectral fit results

Based on the fit statistic and on the reliability of the best-fit parameters, we believe that the ‘decoupled’ `MYTorus` in “edge-on” configuration is the best-fit model for NGC 1358. In our fits, all models have good statistic,

with $\chi_\nu \sim 0.9$ – 1.1 , nonetheless their physical interpretation varies significantly. For example, model B suggests a reflection dominated scenario; in both the ‘coupled’ `MYTorus` and ‘decoupled’ `MYTorus` in “face-on” configuration, the Compton-scattered component contribution to the total observed emission is as significant as the direct continuum one; finally, the ‘decoupled’ `MYTorus` in “edge-on” configuration, which gives the best statistic, suggests that the direct continuum dominates at $E > 10 \text{ keV}$ and the contribution of the reprocessed component is relatively smaller, and a similar result is also obtained using `borus02`.

We are going to use ‘decoupled’ `MYTorus` in “edge-on” configuration as a reference in the rest of the paper because it allows one to compute the iron $K\alpha$ line equivalent width, which cannot be done as straightforwardly using `borus02`, whose iron $K\alpha$ line and the reprocessed component are coupled together. The only exception will be in Section 4.3, where the results of the `borus02` model, in which f_c is a free parameter, will be used in discussing the torus covering factor; however, as mentioned above, the best-fit results of `borus02` are in full agreement with those of the ‘decoupled’ `MYTorus` in “edge-on” configuration.

3.4. Flux and Column Density Variability

While the majority of tori models, such as `MYTorus` and `borus02`, assume a uniform distribution of the obscuring material, several works in the last 25 years have shown that a clumpy distribution of optically thick clouds, the so-called “patchy torus”, is in fact a scenario favored by the observations (see, e.g., Krolik & Begelman 1988; Antonucci 1993; Jaffe et al. 2004; Elitzur & Shlosman 2006; Nenkova et al. 2008).

Mendoza-Castrejón et al. (2015) study the silicates spectral features at 10 and 18 μm in MIR band, showing that the distribution of the obscuring material around the SMBH has a clumpy structure. Following this scenario, it may be possible to observe changes of the “line-of-sight” column density, $N_{\text{H,Z}}$, with time. For this purpose, we divide our *NuSTAR* and XMM-*Newton* observations into several shorter observations and extract a spectrum for each of them having at least ~ 150 net counts (except for the first pn observation, which has 75 net counts, due to a background flare at the beginning of the XMM-*Newton* observation).

Since the XMM-*Newton* observation started ~ 13 hours after the *NuSTAR* one, we divide our *NuSTAR* and XMM-*Newton* observations into three blocks: *i*) The first one contains the 26 ks of *NuSTAR* observation taken before the beginning of the XMM-*Newton* observation. *ii*) The second and third ones are obtained dividing the remaining 24 ks of *NuSTAR* data and the 48 ks XMM-*Newton* data in two even pieces, each one includes 12 ks *NuSTAR* observation and 24 ks of XMM-*Newton* observation. We remind that the *NuSTAR* observation was taken in blocks of ~ 3 ks each, therefore the *NuSTAR* and XMM-*Newton* observations start at different time but finish at the same time. The background subtracted *NuSTAR* FPMA and XMM-*Newton* MOS1 light curves of NGC 1358 are shown in Figure 4 and Figure 5.

The three spectra are fitted with the phenomenological model, since we are mostly interested in measuring flux and/or column density variation. We report in Table

Table 3
Physical properties in different time ranges. Fit performed with phenomenological model

Observation	Overall observations	0-26 ks NuSTAR	26-38 ks NuSTAR & 0-24 ks XMM	38-50 ks NuSTAR & 24-48 ks XMM
χ^2/dof	256/240	84/94	92/87	66/85
Γ	$1.14^{+0.12}_{-0.13}$	$1.48^{+0.24}_{-0.25}$	$1.30^{+0.23}_{-0.21}$	$1.27^{+0.26}_{-0.25}$
N_H^a	$0.95^{+0.11}_{-0.11}$	$1.41^{+0.30}_{-0.29}$	$1.15^{+0.20}_{-0.18}$	$1.06^{+0.19}_{-0.18}$
$F_{-10 \text{ keV}}^b$	$4.18^{+0.23}_{-0.59}$	$5.15^{+0.46}_{-2.36}$	$4.14^{+0.38}_{-2.17}$	$4.39^{+0.48}_{-1.71}$

^aunits of all column density are 10^{24} cm^{-2}

^b2-10 keV observe flux $10^{-13} \text{ erg cm}^2 \text{ s}^{-1}$

3 the best-fit Γ , N_H and flux of 2–10 keV for each of the three sub-observations. The flux and column density measured in the different blocks are consistent with each other, although those of block 1 are marginally offset with respect to the other two, a result that is mostly due to a calibration offset between *XMM-Newton* and *NuSTAR*. In fact, when fitting the block 2 and 3 *NuSTAR* data alone we find a smaller discrepancy and the results are in agreement at 90% confidence level.

We also plot the contour of photon index and column density in Figure 6, where the red, green and blue lines are at 68%, 90% and 99% confidence level. Time blocks 1 to 3 are plotted in solid, dash and dot lines respectively. As can be seen, both quantities are consistent among the three blocks, at a 90% confidence level.

Finally, we fit the *NuSTAR* 3–79 keV light curve (Figure 4) with a constant corresponding to the average count rate of our source, which is $r = 2.3 \pm 0.3 \times 10^{-2} \text{ cts s}^{-1}$. The best-fit statistic is $\chi^2 = 9.3$, and the fit has 10 degrees of freedom. At 99% confidence level, the light curve is strongly different from a constant if $\chi^2 > 23.2$. We repeat the above process for the 0.6–10 keV background subtracted light curve of *XMM-Newton* MOS1 module (Figure 5). The average count rate is $r = 9.8 \pm 1.6 \times 10^{-3} \text{ cts s}^{-1}$ and the best-fit statistic is $\chi^2 = 19.0$ with 9 degrees of freedom. At 99% confidence level, the light curve is strongly different from a constant if $\chi^2 > 21.7$. Therefore, we find no obvious evidence of variability in either flux or absorbing column density.

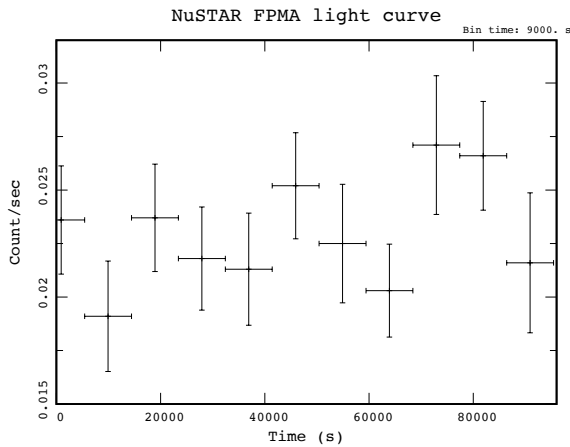


Figure 4. Background subtracted light curve of *NuSTAR* module FPMA. The bin time equals to 9 ks. The average count rate is $r = 2.3 \pm 0.3 \times 10^{-2} \text{ cts s}^{-1}$.

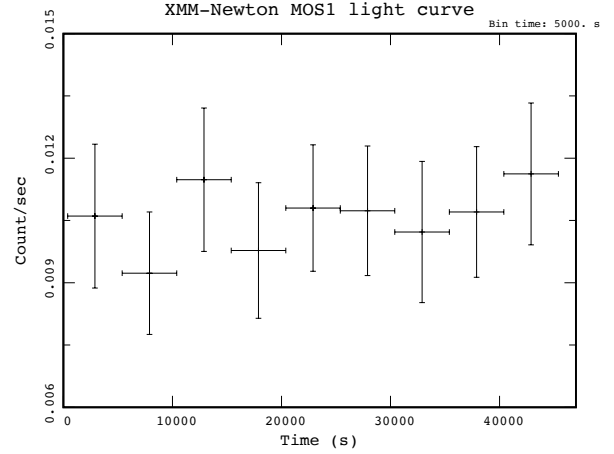


Figure 5. Background subtracted light curve of *XMM-Newton* MOS1. The bin time equals to 5 ks. The average count rate is $r = 9.8 \pm 1.6 \times 10^{-3} \text{ cts s}^{-1}$.

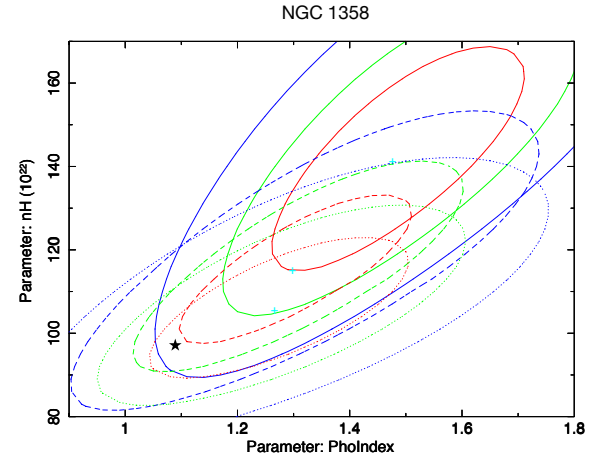


Figure 6. Contour of photon index and column density of three time blocks fitted with phenomenological model. The red, green and blue lines are at 68%, 90% and 99% confidence level. Contours of time blocks 1 to 3 are solid, dash and dot lines respectively. The photon index and column density of the overall observations is marked as a black star.

3.5. Equivalent width of the iron $K\alpha$ line

Thanks to the excellent count statistics provided by *NuSTAR* and *XMM-Newton* in the 5–8 keV band, we were also able to place strong constraints on the Fe $K\alpha$ line equivalent width (EW), a significant improve-

ment with respect to Marchesi et al. (2017a), where only an upper limit on EW could be derived. We measure equivalent width $EW_{\text{pow}} = 0.72^{+0.16}_{-0.16}$ keV and $EW_{\text{pex}} = 0.63^{+0.15}_{-0.14}$ keV using the model A and model B respectively.

To measure the Fe K α line EW with MYTorus we use the approach described in Yaqoob et al. (2015). We therefore first measure the continuum flux, without including the emission line, at $E_{K\alpha} = 6.4$ keV. We then compute the flux of the fluorescent lines component in the energy range $E = [0.95 E_{K\alpha} - 1.05 E_{K\alpha}]$, i.e., between 6.08 and 6.72 keV, rest-frame. EW is then computed by multiplying by $(1 + z)$ the ratio between the fluorescent line flux and the monochromatic continuum flux. We obtain $EW_{\text{coupl}} = 0.69^{+0.13}_{-0.12}$ keV, $EW_{\text{decoupl}, \theta=90} = 0.70^{+0.14}_{-0.11}$ keV and $EW_{\text{decoupl}, \theta=0} = 0.65^{+0.12}_{-0.13}$ keV, such that all the MYTorus EW values are in good agreement with those obtained in the phenomenological model.

4. DISCUSSION AND CONCLUSIONS

4.1. Compared with previous results

In this work, we report the results of the spectral analysis of quasi-simultaneous *NuSTAR* (50 ks) and XMM-*Newton* (48 ks) observations of NGC 1358, a nearby Seyfert 2 galaxy, which was recently found to be a CT-AGN candidate (Marchesi et al. 2017a) based on its combined *Swift*-BAT and *Chandra* spectrum. The limited quality of the *Chandra* and *Swift*-BAT spectra was reflected in the rather large (~ 30 – 40%) 90% confidence parameter uncertainties, and NGC 1358 Compton thickness could not be validated beyond the 1σ confidence level. More in detail, Marchesi et al. (2017a) used MYTorus ‘coupled’ configuration to model the combined *Chandra*-*Swift*-BAT spectrum of NGC 1358. Their best-fit ($\chi^2/\text{d.o.f.} = 14.8/13$) gave a column density of $N_{\text{H,Z}} = 1.05^{+0.42}_{-0.36} \times 10^{24} \text{ cm}^{-2}$ assuming the inclination angle to be $\theta_{\text{obs}} = 90^\circ$.

NGC 1358 was first reported as a candidate CT-AGN by Marinucci et al. (2012), which measured the X-ray spectral properties of NGC 1358 by fitting a 2–10 keV XMM-*Newton* spectrum observed in 2005 (exposure time 12.7 ks) with a Compton-reflection model (pexrav). The column density they obtained is $N_{\text{H,Z}} = 1.30^{+8.50}_{-0.60} \times 10^{24} \text{ cm}^{-2}$, in good agreement with the findings of Marchesi et al. (2017a). Once again, the CT- nature of NGC 1358 was not confirmed at a $>1\sigma$ significance level.

The first main result of our analysis is therefore that NGC 1358 is a confirmed, *bona-fide* Compton-Thick AGN, based on the two models which provide the most reliable fit, i.e., the ‘decoupled’ MYTorus model in “edge on” configuration and borus02 model. More in detail, our best-fit “line-of-sight” column density obtained by the MYTorus ‘decoupled’ model in “edge on” configuration is $N_{\text{H,Z}} = 2.40^{+0.40}_{-0.44} \times 10^{24} \text{ cm}^{-2}$ and for most of the parameters, the uncertainties are $<20\%$ at 90% confidence.

4.2. Intrinsic X-ray luminosity

In table 2, we report the observed flux and intrinsic luminosity of NGC 1358 in the 2–10 keV and 10–40 keV energy ranges, for all the different models discussed in Section 3. The observed flux values are consistent among

both the phenomenological and the physical models, in both energy ranges. We instead observe significant differences between the best-fit luminosity values, since the ‘decoupled’ MYTorus model in “edge-on” configuration and the borus02 model give a 2–10 keV intrinsic luminosity $L_{2-10 \text{ keV}} \sim 2.06 \times 10^{43} \text{ erg s}^{-1}$, while the intrinsic luminosity in 2–10 keV for the other models is $L_{2-10 \text{ keV}} < 0.4 \times 10^{43} \text{ erg s}^{-1}$, which is at least 6 times smaller than the best-fit models. This large difference is a direct consequence of the fits results: in the phenomenological models, the “coupled” MYTorus model and the “decoupled” MYTorus ‘face-on’ model, NGC 1358 is intrinsically less luminous, has a harder (somehow unphysical, particularly in the phenomenological model) photon index, is less obscured and has a strong reprocessed component. In the “decoupled” MYTorus ‘edge-on’ model and in borus02, instead, NGC 1358 is more luminous, more obscured, has a softer, more typical photon index, and the reprocessed component is relative small.

Moreover, the intrinsic X-ray luminosity can also be inferred from luminosities derived at different wavelengths, e.g., the middle infrared (MIR) luminosity (see, e.g., Elvis et al. 1978) and the [OIII] luminosity (see, e.g., Heckman et al. 2005). The MIR luminosity of NGC 1358 is obtained by using the flux at $12 \mu\text{m}$, $F_{12\mu\text{m}} = 1.43 \pm 0.03 \times 10^{-2} \text{ Jy}$ (Wright et al. 2010): the corresponding luminosity is $L_{12\mu\text{m}} = 1.23 \pm 0.03 \times 10^{42} \text{ erg s}^{-1}$. Using the $L_{\text{MIR}}\text{--}L_{2-10 \text{ keV}}$ relation in Asmus et al. (2015), we then obtain the MIR-inferred X-ray intrinsic luminosity $L_{2-10 \text{ keV, MIR}} \sim 5.2 \times 10^{41} \text{ erg s}^{-1}$. The [OIII] luminosity of NGC 1358 is reported in Whittle (1992) and is $L_{[\text{OIII}]} = 9.8 \times 10^{40} \text{ erg s}^{-1}$. Applying the $L_{[\text{OIII}]}\text{--}L_{2-10 \text{ keV}}$ relation from Georgantopoulos & Akylas (2010), we obtain the [OIII]-inferred X-ray intrinsic luminosity $L_{2-10 \text{ keV, [OIII]}} \sim 5.31 \times 10^{42} \text{ erg s}^{-1}$. Notably, these luminosities are in better agreement with those computed using the phenomenological models, the ‘coupled’ MYTorus model and the ‘decoupled’ MYTorus model in “face-on” configuration, rather than with that derived using the ‘decoupled’, “edge-on” MYTorus model that we selected as our best-fit model. However, we point out that both $L_{\text{MIR}}\text{--}L_{2-10 \text{ keV}}$ and the $L_{[\text{OIII}]}\text{--}L_{2-10 \text{ keV}}$ relations are derived using phenomenological models, which are known to be less reliable than the physical models when fitting the heavily obscured AGN, such as NGC 1358. The low MIR luminosity reported above may be due to the low covering factor of the torus in NGC 1358 (see next section). However, despite being disfavored by the data, the possibility that the source is less obscured and intrinsically fainter than suggested by the best-fit model cannot be ruled out.

4.3. Covering factor

One of the advantages in fitting the X-ray spectra of heavily obscured AGNs using a physical model is the possibility to measure specific tori parameters, such as the torus covering factor, f_c . In borus02 the covering factor is a free parameter: we find that the best-fit borus02 solution supports a low- f_c scenario for NGC 1358, with $f_c < 0.17$, thus suggesting a “disk-like” torus. Such an evidence is supported also by the MYTorus best-fit model: in fact, while in MYTorus f_c is not a free parameter, the ratio between the normalization of the intrinsic continuum and

the one of the Compton-scattered continuum, A_S , can be used as a proxy of the torus covering factor. More in detail, from our best-fit **MYTorus** model, i.e., the ‘decoupled edge on’ one, we obtain $A_S = 0.23^{+0.18}_{-0.06}$. The estimated covering factor is then $f_c = 0.5 \times A_S = 0.12^{+0.09}_{-0.03}$, again supporting a “disk-like” torus scenario. However, it is worth mentioning that Yaqoob (2012) points out that the existence of a non-negligible time delay between the two components can also result in the relative normalization being away from unity.

Finally, we checked for further evidence of a “disk-like” torus scenario using the ratio of the torus luminosity to the AGN luminosity as a proxy of the torus covering factor (Stalevski et al. 2016). We indirectly infer the torus luminosity from the $12\mu\text{m}$ luminosity, which is dominated by the emission reprocessed by the torus. We can then derive a first order estimate of the dust torus covering factor, $f_c = L_{\text{tor}}/L_{\text{bol}} \sim 0.005$, where L_{tor} is the torus luminosity and $L_{\text{bol}} = 2.34 \times 10^{44} \text{ erg s}^{-1}$ (Woo & Urry 2002) is the bolometric luminosity of the AGN. While this result needs to be validated by a more accurate modeling and fit of the torus SED, it still points to a “disk-like” torus scenario.

4.4. Clumpiness of the torus

In section 3.2, we computed both the “line-of-sight” column density, $N_{\text{H,Z}}$, and the torus “global average” column density, $N_{\text{H,S}}$, using both **MYTorus** in its ‘decoupled’ configuration, and **borus02**. In both cases, we find a mild (~ 4 times) difference between the “line-of-sight” column density and the torus “global average” column density, an evidence which supports an inhomogeneous distribution of the obscuring material surrounding the accreting SMBH in NGC 1358. We point out that this statement may seem in contradiction with what we stated in Section 3.2.3 when presenting the **MYTorus** decoupled “face-on” model, i.e., the fact that the “face-on” model, rather than the “edge-on” one, should be more effective in characterizing a patchy torus scenario, where there is a higher chance to observe the reprocessed emission coming from the “back-side” of the torus. However, this potential discrepancy can be explained assuming that in NGC 1358 the torus covering factor is indeed small, and the reprocessed component contribution to the overall observed emission is therefore small: consequently, since the “back-side” reprocessed component is expected to be a fraction of the front-side one, in this specific case it is basically negligible.

To further investigate this potential “patchy torus” scenario, in Section 3.4 we divide our *NuSTAR* and *XMM-Newton* observations into three blocks and fit each of the sub-observations. As can be seen in Table 3, all the parameters are in agreement within the uncertainties, and no variability is therefore detected. This suggests that the timescale associated to a significant positional change of the clouds within the torus is much larger than $\sim 50 \text{ ks}$ or that the torus is more uniformly distributed than what the best-fit model suggests. However, the lack of significant variability in a 50 ks observation provides us with a way to set a lower limit on the size of obscuring clouds. Assuming that the obscuring clouds are $r = 1 \text{ pc}$ away from the accreting SMBH (see e.g., ?). The mass of the super massive black hole in NGC

1358 is $\log(M_{\text{BH}}/M_{\odot}) = 7.88$ (Woo & Urry 2002), such that the velocity of the clouds is $v_{\text{cloud}} = (GM_{\text{BH}}/r)^{1/2} = 570 \text{ km s}^{-1}$, which is in line with the FWHM velocity obtained from the velocity broadening of the emission lines. Therefore, the lower limit to the radius of the obscuring cloud should be $R_{\text{cloud}} = v_{\text{cloud}} \times 50 \text{ ks} = 3 \times 10^7 \text{ km} \sim 43 R_{\odot}$.

4.5. Eddington ratio and mass accretion rate

Finally, we analyzed our X-ray data to derive the Eddington ratio and mass accretion rate of the SMBH in NGC 1358. The Eddington ratio is a measurement of the SMBH accretion efficiency, and is defined as $\lambda_{\text{Edd}} = L_{\text{bol}}/L_{\text{Edd}}$, i.e., as the ratio between the bolometric luminosity, L_{bol} , and the so-called Eddington luminosity, $L_{\text{Edd}} = 4\pi GM_{\text{BH}}m_p c/\sigma_T$, where M_{BH} is the SMBH mass and m_p is the mass of proton.

Woo & Urry (2002) report a measurement of both the black hole mass and the bolometric luminosity of NGC 1358. The mass of the black hole is obtained by the correlation between the black hole mass with stellar velocity dispersion, and the bolometric luminosity is obtained through direct integration of the spectral energy distribution. Based on these values, the Eddington ratio of NGC 1358 is $\lambda_{\text{Edd}} = 2.5 \times 10^{-2}$.

Our high-quality X-ray data allows us to recompute L_{bol} , extrapolating it from our best-fit 2–10 keV intrinsic luminosity, $L_{\text{int},2-10 \text{ keV}} = 2.06^{+0.11}_{-0.11} \times 10^{43} \text{ erg s}^{-1}$. We use the bolometric correction of Marconi et al. (2004, Equation 21), finding a bolometric luminosity $L_{\text{bol}} = 4.36^{+0.29}_{-0.30} \times 10^{44} \text{ erg s}^{-1}$. Thus the corresponding Eddington efficiency is $\lambda_{\text{Edd}} \sim 4.7^{+0.3}_{-0.3} \times 10^{-2}$, which is typical for AGN in the range $[0.001-1]$, using the black hole mass value from Woo & Urry (2002). This result is also consistent with Marinucci et al. (2012), which reported an Eddington ratio of $\lambda_{\text{Edd}} = 1.62 \times 10^{-2}$, relying on an estimate of the black hole mass of $\log(M_{\text{BH}}/M_{\odot}) = 7.99$, and a bolometric luminosity, $L_{\text{bol}} = 2.04 \times 10^{44} \text{ erg s}^{-1}$.

Schnorr-Müller et al. (2017) estimated a NGC 1358 ionized mass inflow rate (excluding the neutral and molecular gas, being only the lower limit of the total mass inflow) of $\dot{M}_{\text{in}} \approx 1.5 \times 10^{-2} M_{\odot} \text{ yr}^{-1}$ in the inner 180 pc. The authors also report the mass accretion rate, obtained using the [OIII] luminosity from Gu & Huang (2002) and the bolometric correction from Lamastra et al. (2009), being $\dot{m}_{\text{acc}} \sim 0.9 \times 10^{-4} M_{\odot} \text{ yr}^{-1}$, which is 160 times smaller than the mass inflow rate of NGC 1358. According to the relationship between the mass accretion rate and the bolometric luminosity, $\dot{m}_{\text{acc}} = L_{\text{bol}}/\eta c^2$, where η is the efficiency that converts the rest mass energy of accreted material into radiation and is assumed to be $\eta = 0.1$ (Frank et al. 2002), we also estimate the mass accretion rate in NGC 1358, which is $\dot{m}_{\text{acc}} = [7.2-8.2] \times 10^{-2} M_{\odot} \text{ yr}^{-1}$ adopting the bolometric luminosity from our best-fit, which is in the same order with the mass inflow rate reported in Schnorr-Müller et al. (2017): the large difference between the mass accretion rate and the mass inflow rate reported in Schnorr-Müller et al. (2017) could be diminished when the bolometric luminosity is measured from the 2–10 keV X-ray band rather than from the [OIII] luminosity.

As shown here, *NuSTAR* and *XMM-Newton* are instru-

mental to identify and study CT-AGNs in details. We envision that extending these studies to most CT-AGN known in the Local Universe will allow us to shed light on the, so far elusive, population of CT-AGN.

X.Z. thanks the referee for their detailed and useful comments, which helped in significantly improving the paper. X.Z., S.M. and M.A. acknowledge NASA funding under contract 80NSSC17K0635. *NuSTAR* is a project led by the California Institute of Technology (Caltech), managed by the Jet Propulsion Laboratory (JPL), and funded by the National Aeronautics and Space Administration (NASA). We thank the NuSTAR Operations, Software and Calibrations teams for support with these observations. This research has made use of the NuSTAR Data Analysis Software (NuSTARDAS) jointly developed by the ASI Science Data Center (ASDC, Italy) and the California Institute of Technology (USA). This research has made use of data and/or software provided by the High Energy Astrophysics Science Archive Research Center (HEASARC), which is a service of the Astrophysics Science Division at NASA/GSFC and the High Energy Astrophysics Division of the Smithsonian Astrophysical Observatory.

REFERENCES

- Ajello, M., Greiner, J., Sato, G., et al. 2008, *The Astrophysical Journal*, 689, 666
- Alexander, D. M., Bauer, F. E., Brandt, W. N., et al. 2003, *The Astronomical Journal*, 126, 539
- Almeida, C. R. & Ricci, C. 2017, *Nature Astronomy*, 1, 679
- Anders, E. & Grevesse, N. 1989, *Geochimica et Cosmochimica Acta*, 53, 197
- Annuar, A., Alexander, D. M., Gandhi, P., et al. 2017, *The Astrophysical Journal*, 836, 165
- Annuar, A., Gandhi, P., Alexander, D. M., et al. 2015, *The Astrophysical Journal*, 815, 36
- Antonucci, R. 1993, *Annu. Rev. Astron. Astrophys.*, 31, 473
- Arnaud, K. A. 1996, *Astronomical Data Analysis Software and Systems V*, 101, 17
- Asmus, D., Gandhi, P., Hönig, S. F., Smette, A., & Duschl, W. J. 2015, *Monthly Notices of the Royal Astronomical Society*, 454, 766
- Baloković, M., Brightman, M., Harrison, F. A., et al. 2018, *The Astrophysical Journal*, 854, 42
- Baloković, M., Comastri, A., Harrison, F. A., et al. 2014, *The Astrophysical Journal*, 794, 111
- Barthelmy, S. D., Barbier, L. M., Cummings, J. R., et al. 2005, *Space Science Reviews*, 120, 143
- Bauer, F. E., Arévalo, P., Walton, D. J., et al. 2015, *The Astrophysical Journal*, 812, 116
- Boller, T., Freyberg, M. J., Trümper, J., et al. 2016, *A&A*, 588, A103
- Brightman, M. & Nandra, K. 2011, *Monthly Notices of the Royal Astronomical Society*, 413, 1206
- Buchner, J., Georgakakis, A., Nandra, K., et al. 2015, *The Astrophysical Journal*, 802, 89
- Burlon, D., Ajello, M., Greiner, J., et al. 2011, *The Astrophysical Journal*, 728, 58
- Elitzur, M. & Shlosman, I. 2006, *The Astrophysical Journal Letters*, 648, L101
- Elvis, M., Maccacaro, T., Wilson, A. S., et al. 1978, *Monthly Notices of the Royal Astronomical Society*, 183, 129
- Frank, J., King, A., & Raine, D. J. 2002, *Accretion Power in Astrophysics: Third Edition* (Cambridge, UK: Cambridge University Press)
- Furui, S., Fukazawa, Y., Odaka, H., et al. 2016, *The Astrophysical Journal*, 818, 164
- Gandhi, P. & Fabian, A. C. 2003, *Monthly Notices of the Royal Astronomical Society*, 339, 1095
- Georgantopoulos, I. & Akylas, A. 2010, *A&A*, 509, A38
- Georgantopoulos, I., Comastri, A., Vignali, C., et al. 2013, *A&A*, 555, A43
- Gilli, R., Comastri, A., & Hasinger, G. 2007, *A&A*, 463, 79
- Gu, Q. & Huang, J. 2002, *The Astrophysical Journal*, 579, 205
- Harrison, F. A., Craig, W. W., Christensen, F. E., et al. 2013, *The Astrophysical Journal*, 770, 103
- Heckman, T. M., Ptak, A., Hornschemeier, A., & Kauffmann, G. 2005, *The Astrophysical Journal*, 634, 161
- Ikeda, S., Awaki, H., & Terashima, Y. 2009, *The Astrophysical Journal*, 692, 608
- Jaffe, W., Meisenheimer, K., Röttgering, H. J. A., et al. 2004, *Nature*, 429, 47 EP
- Jansen, F., Lumb, D., Altieri, B., et al. 2001, *A&A*, 365, L1
- Kalberla, P. M. W., Burton, W. B., Hartmann, Dap, et al. 2005, *A&A*, 440, 775
- Koss, M. J., Assef, R., Baloković, M., et al. 2016, *The Astrophysical Journal*, 825, 85
- Krolik, J. H. & Begelman, M. C. 1988, *Astrophysical Journal*, 329, 702
- Lamastra, A., Bianchi, S., Matt, G., et al. 2009, *A&A*, 504, 73
- Lanzuisi, G., Ranalli, P., Georgantopoulos, I., et al. 2015, *A&A*, 573, A137
- Liu, Y. & Li, X. 2014, *The Astrophysical Journal*, 787, 52
- Magdziarz, P. & Zdziarski, A. A. 1995, *Monthly Notices of the Royal Astronomical Society*, 273, 837
- Marchesi, S., Ajello, M., Comastri, A., et al. 2017a, *The Astrophysical Journal*, 836, 116
- Marchesi, S., Ajello, M., Marcotulli, L., et al. 2018, *The Astrophysical Journal*, 854, 49
- Marchesi, S., Lanzuisi, G., Civano, F., et al. 2016, *The Astrophysical Journal*, 830, 100
- Marchesi, S., Tremblay, L., Ajello, M., et al. 2017b, *The Astrophysical Journal*, 848, 53
- Marconi, A., Risaliti, G., Gilli, R., et al. 2004, *Monthly Notices of the Royal Astronomical Society*, 351, 169
- Marinucci, A., Bianchi, S., Nicastro, F., Matt, G., & Goulding, A. D. 2012, *The Astrophysical Journal*, 748, 130
- Matt, G. & Fabian, A. C. 1994, *Monthly Notices of the Royal Astronomical Society*, 267, 187
- Mendoza-Castrejón, S., Dultzin, D., Krongold, Y., González, J. J., & Elitzur, M. 2015, *Monthly Notices of the Royal Astronomical Society*, 447, 2437
- Mewe, R., Gronenschild, E. H. B. M., & van den Oord, G. H. J. 1985, *A&AS*, 62, 197
- Murphy, K. D. & Yaqoob, T. 2009, *Monthly Notices of the Royal Astronomical Society*, 397, 1549
- Nenkova, M., Sirocky, M. M., Ivezić, Ž., & Elitzur, M. 2008, *The Astrophysical Journal*, 685, 147
- Puccetti, S., Comastri, A., Fiore, F., et al. 2014, *The Astrophysical Journal*, 793, 26
- Ricci, C., Ueda, Y., Koss, M. J., et al. 2015, *The Astrophysical Journal Letters*, 815, L13
- Ricci, C., Walter, R., Courvoisier, T. J.-L., & Paltani, S. 2011, *A&A*, 532, A102
- Risaliti, G., Maiolino, R., & Salvati, M. 1999, *The Astrophysical Journal*, 522, 157
- Schnorr-Müller, A., Storchi-Bergmann, T., Nagar, N. M., Robinson, A., & Lena, D. 2017, *Monthly Notices of the Royal Astronomical Society*, 471, 3888
- Stalevski, M., Ricci, C., Ueda, Y., et al. 2016, *Monthly Notices of the Royal Astronomical Society*, 458, 2288
- Theureau, G., Bottinelli, L., Coudreau-Durand, N., et al. 1998, *Astron. Astrophys. Suppl. Ser.*, 130, 333
- Treister, E., Urry, C. M., & Virani, S. 2009, *The Astrophysical Journal*, 696, 110
- Ueda, Y., Akiyama, M., Hasinger, G., Miyaji, T., & Watson, M. G. 2014, *The Astrophysical Journal*, 786, 104
- Ursini, F., Bassani, L., Panessa, F., et al. 2018, *Monthly Notices of the Royal Astronomical Society*, 474, 5684
- Verner, D., Ferland, G., Korista, K., & Yakovlev, D. 1996, *Astrophysical Journal*, 465, 487
- Whittle, M. 1992, *ApJS*, 79, 49
- Winkler, C., T. J.-L. Courvoisier, Di Cocco, G., et al. 2003, *A&A*, 411, L1
- Woo, J.-H. & Urry, C. M. 2002, *The Astrophysical Journal*, 579, 530

- Wright, E. L., Eisenhardt, P. R. M., Mainzer, A. K., et al. 2010, The Astronomical Journal, 140, 1868
- Yaqoob, T. 2012, Monthly Notices of the Royal Astronomical Society, 423, 3360
- Yaqoob, T., Tatum, M. M., Scholtes, A., Gottlieb, A., & Turner, T. J. 2015, Monthly Notices of the Royal Astronomical Society, 454, 973